PAPER

Check for updates

Treatment of chromium-contaminated water using a highly efficient, novel ternary synergistic S–rGO–BiOBr–In2S3 heterojunction

Satyanjib Sahoo,[a] Naresh Kumar Sahoo, [ID] *[a] Prasanta Kumar Sahoo,[b] Soumya Mishra,[a] Arun Kumar,[c] Brundabana Naik [ID] [a] and Prangya Ranjan Rout[d]

The goal of the current study is to form a Z-scheme heterojunction between narrow band gap In2S3 (indium sulphide) and wide band gap BiOBr (bismuth oxobromide) to minimize the photoinduced charge carrier recombination and increase the visible light harvesting capacity of the nanocomposite for Cr(VI) elimination from polluted water. The exfoliated and corrugated S-doped rGO (sulphur-doped graphene oxide) were used to enhance the surface area and conductivity, encourage nucleation, and act as anchor sites for interfacial contact between BiOBr and In2S3 to facilitate efficient charge transfer. In this work, a BiOBr–In2S3–SrGO nanocomposite was successfully synthesized by a facile hydrothermal method. The optical and physicochemical properties of the synthesized nanomaterials (NMs) were characterized using XRD, FTIR, FE-SEM, EDAX, HRTEM, XPS, UV-DRS, Raman and photoluminescence spectroscopy. The results reveal that almost 96.6% Cr(VI) removal was achieved from an initial Cr(VI) dose of 100 mg L^{-1} by the nanocomposite within 2 h under the illumination of solar light. On the other hand, the Cr(VI) reduction was limited to 33.4% and 30.9% using the individual NMs of BiOBr and In2S3, respectively. The reduction of Cr(VI) follows pseudo-first-order kinetics. The calculated apparent rate constant (K_{app}) of the nanocomposite was 3 times more than the individual NMs of BiOBr and In2S3, with an excellent recycling activity.

1. Introduction

Chromium (Cr(VI)) is highly toxic and bio-accumulates in the food chain. Its presence in natural water and industrial wastewater streams is a significant environmental and public health risk.[1] Furthermore, among the hazardous environmental pollutants, Cr(VI) ranked third and is released from effluents of a number of industries; for example: electroplating, textile, dying, tanning nuclear power, and photographic sectors.[2] According to recent reports, wastewater typically contains 10–100 mg L^{-1} of Cr(VI).[3] As per the World Health Organization (WHO), the permissible limit of Cr(VI) is less than 0.05 mg L^{-1} in drinking water.[4] In general, Cr(VI) penetrates the cell wall quickly, causing cancer, and damage to the liver, kidneys, and

nerve tissue.[5] Several techniques have been reported to remove Cr(VI), including ion exchange, chemical precipitation, electrochemical processes, membrane filtration, and adsorption methods. These methods have many drawbacks, including the fouling of membranes, production of carcinogenic by-products, ineffective removal, and high cost.[6] One of the most promising methods for the effective removal of Cr(VI) is the reduction of Cr(VI) to Cr(III) because Cr(III) is less toxic, and can be easily precipitated and removed as Cr(OH)$_3$ from contaminated water.[7] Compared with other methods, photocatalytic reduction of Cr(VI) is more effective and low-cost, and does not produce any hazardous by-products.[8] However, many challenges still exist in the photocatalytic reduction process, such as inefficient solar light harvesting, high rate of charge carrier recombination, and inability to remove the high-strength real Cr(VI) wastewater samples. Thus, the photocatalytic reduction process must be improved to meet the discharge standard.[9]

BiOBr is an indirect bandgap semiconductor. The unique electronic structure of BiOBr, especially its abundance of Bi 6s orbitals that come from the conduction band (CB) and valence band (VB), produces a tenable electronic state and high charge mobility that promote higher photocatalytic activity.[10,11] Nevertheless, the primary issue with BiOBr as a photocatalysts is the high band gap energy of 2.81 eV that prevents them from fully

[a] *Department of Chemistry, Environmental Science and Technology Program, Faculty of Engineering and Technology (ITER), Siksha 'O' Anusandhan (Deemed to be University), Bhubaneswar 751030, Odisha, India. E-mail: nareshsahoo@soa.ac.in*

[b] *Environmental Hydrology Division, National Institute of Hydrology, Jalvigyan Bhawan, Roorkee 247667, India*

[c] *Department of Chemistry, Indian Institute of Technology (IIT) Roorkee, Uttarakhand, India*

[d] *Department of BioTechnology, Dr B R Ambedkar National Institute of Technology Jalandhar, Jalandhar, India*

harvesting solar irradiation, especially in the visible spectrum. Furthermore, the low affinity between pollutants and photocatalysts, together with the inadequate specific surface area, inhibit the overall photocatalytic activity.[12] Similarly, In_2S_3 is the ideal choice to enhance the optical characteristics and physical structure of nanomaterials (NMs) for boosting photocatalytic activity. Because of its excellent stability and high photosensitivity, In_2S_3 with a narrow band gap of 2.0–2.3 eV has been employed extensively as a photocatalyst. However, under visible light excitation, the photogenerated holes produced by In_2S_3 can react with S^{2-} of the photocatalyst, resulting in catalyst deactivation.[13] It is also found that In_2S_3 has a low photocatalytic nature due to its low mass transfer and high charge carrier recombination rate. These problems have become a bottleneck for effectively developing and applying sulphide-based semiconductors such as In_2S_3.[14] Hence, in this work, a Z-scheme heterojunction has been fabricated between BiOBr and In_2S_3 to overcome these issues and enhance its photocatalytic efficiency. Similarly, reduced graphene oxide (rGO) is growing in popularity because of its remarkable qualities, which include a high functional group density, an enormous specific surface area (2600 m^2 g^{-1}), excellent electron conductive properties (15 000 m^2 V^{-1} s^{-1}), high chemical and thermal stability, and more. Therefore, it has also been proposed that rGO is an ideal option as a promoter or catalyst carrier. Additionally, the delocalized π electron in sp^2 carbon can increase the electron mobility in rGO.[15] Furthermore, S-doped rGO was used in the nanocomposite to facilitate efficient charge transfer, which encourages nucleation and acts as an anchor site for interfacial contact between BiOBr and In_2S_3. In addition, SrGO can significantly increase the structural stability and reaction kinetics and reduce the photo-generated electron–hole recombination ratio, thus boosting the movement of electrons and ions, especially across the interface.[16]

The present study synthesized a novel S–rGO–BiOBr–In_2S_3 Z-scheme heterojunction using a hydrothermal method to remove Cr(III) from contaminated wastewater. The morphological and structural and elemental characterizations of the NMs were performed using XRD, FTIR, FESEM, EDX, HRTEM, XPS, UV-DRS, photoluminescence, and Raman spectroscopy analysis. The kinetics of Cr(III) removal by the nanocomposite was evaluated, and the Cr(VI) reduction mechanism was thoroughly explained. In addition, the reusability capacity of the nanocomposite for Cr(VI) removal was investigated.

2. Materials and methods

2.1. Materials

Analytical grade Bi $(NO_3)_3 \cdot 5H_2O$, hydrazine hydrate, H_3PO_4, and 1,5-diphenylcarbazide (DPC) were purchased from Merck, India. Graphite powder, $Na_2S \cdot 9H_2O$, was purchased from LOBA chemicals, India, and $In_2O_3 \cdot 5H_2O$ from Burgoyne India. All other chemicals and reagents were of laboratory and analytical grade.

2.2. Methods

2.2.1. Synthesis of BiOBr.
BiOBr was prepared as reported in the literature.[17] Solution A was prepared by dissolving 2.43 g of Bi $(NO_3)_3 \cdot 5H_2O$ and 0.24 g of citric acid in 20 mL of deionized water. Solution B was prepared by dissolving 0.6 g of KBr in 20 ml of ethanol. Then, solution B was dripped into solution A, which was then stirred for 30 min. The resulting solution was kept at 180 °C for 24 h in a hydrothermal autoclave lined with Teflon. The resulting mixture was centrifuged at 10 000 rpm for 10 min. The residue was rinsed with deionised water to remove any potential ionic species, and then dried overnight at 60 °C to obtain the final product.

2.2.2. Synthesis of In_2S_3.
In_2S_3 was produced by hydrothermal methods, as reported in the literature.[18] Solution A was made by dissolving 0.333 g of $In_2O_3 \cdot 5H_2O$ in 40 mL distilled water. In another beaker, 0.720 g $Na_2S \cdot 9H_2O$ was dissolved in 40 ml distilled water, named solution B. After being fully dissolved, solution B was added dropwise to solution A. The pH of the resultant reaction mixture was adjusted to 2.8 by adding diluted HNO_3. The resulting solution was then kept at 180 °C for 24 h in an autoclave lined with Teflon. Then, the acquired orange precipitate was frequently rinsed with deionized water and ethanol. It was then dried for 12 h at 90 °C in a vacuum oven to obtain the final In_2S_3 NMs.

2.2.3. Synthesis of SrGO.
Graphite oxide was prepared using a modified Hummers' process.[15] In an ice bath, 80 mL of cold, concentrated H_2SO_4 was mixed with 2 g of graphite powder. Then 4 g of $NaNO_3$ and 8 g of $KMnO_4$ were added slowly under continuous stirring for 4 h at 10 °C. The mixture temperature was then retained at 35 °C for 4 h. Furthermore, the resultant slurry was diluted with 200 mL of deionized water and stirred for another 1 h. 15 mL of 30% H_2O_2 solution was added to stop the reaction. The resulting GO mixture was centrifuged at 10 000 rpm for 10 min and rinsed a number of times with water and 100% ethanol. The obtained product was then dried in a vacuum oven at 50 °C for 24 h. The SrGO was synthesized according to Tian et al.[19] 1 g of earlier prepared GO was dissolved in 300 mL distilled water and sonicated for 20 min. After that the solution was purged with nitrogen gas for 10 min. Then, 0.5 mL of hydrazine hydrate was mixed with the solution and sonicated for another 10 min. Then, 3 g of Na_2S was added to the solution. The obtained solution was refluxed at 80 °C for 8 h. Then, the acquired residue was repetitively rinsed with deionized water and ethanol and dried at 65 °C in a vacuum oven.

2.2.4. Synthesis of the BiOBr/In_2S_3/SrGO nanocomposite.
A BiOBr–In_2S_3–SrGO heterostructure was prepared using the hydrothermal technique. Solution A was prepared by taking 0.333 g $In_2O_3 \cdot 5H_2O$ in 40 mL of distilled water. Solution B was prepared by dissolving 0.720 g $Na_2S \cdot 9H_2O$ in 40 mL distilled water. After being fully dissolved, solution B was added dropwise to solution A. 330 mg of BiOBr and 500 mg of SrGO were added to the sample. The pH of the solution was retained at 2.8 using diluted nitric acid and then sonicated for 15 min. The resulting solution was then kept at 180 °C for 24 h in an autoclave lined with Teflon. The obtained product was

centrifuged at 10 000 rpm for 15 min. The residue was collected, repetitively rinsed with deionised water and ethanol, and then dried for 12 h at 90 °C in a vacuum oven to obtain the final nanocomposite.

2.2.5. Experimental set up. The Cr(VI) removal activity of the synthesised NMs was assessed under the irradiation of solar light. 5 separate 25 mL conical flasks were filled with 25, 50, 100, 150, and 200 mg L^{-1} Cr(VI) solutions. To eliminate dissolved oxygen, from each flask N$_2$ gas was sparged for 5 min. Then, 1 g L^{-1}, *i.e.* 25 mg of BiOBr–In$_2$S$_3$–SrGO nanocomposite, was supplemented to each flask containing 25 ml of solution. In another conical flask, a 100 mg L^{-1} Cr(VI) solution was taken without adding nanocomposite and labelled as a control solution. All the conical flasks containing Cr(VI) solution were kept in dark conditions for 15 min. After that, the photocatalytic experiment was conducted with continuous stirring under solar irradiation. Sample solutions from each flask were collected at regular intervals and centrifuged at 10 000 rpm for 15 min. The collected supernatants were employed to measure the remaining Cr(VI) concentration.

2.2.6. Analytical method. In order to validate the precise synthesis of the NMs, an X-ray powder diffractometer with a CuKα (λ = 1.5405 Å) radiation source was used to perform XRD analysis across a wide range of Bragg's angles ($20° \leq 2\theta \leq 80°$) (Model: Rikagu Ultima Japan). The Miller indices, unit cell parameters, and crystal structure of the NMs were all computed employing the X'Pert Highscore Plus software. The molecular vibration and functional groups of the synthesized NMs were investigated by FTIR analysis (Jasco FT/IR-4600 LE, Varian spectrophotometer). The prepared NMs structural configuration and vibrational modes were studied using a Raman microscope equipped with a green 532 nm laser (Renishaw Invia). Using photoluminescence (PL) spectra, the recombination of photo-generated charge carriers was investigated (Edinburgh FLS 1000) at 488 nm, 532 nm, 633 nm, and 785 nm excitation wavelengths. The NM morphology, size, and distribution were examined using FE-SEM Gemini SEM 450 equipment with LaB6 and tungsten as the filament source. The energy dispersive X-ray spectroscopy (EDAX) equipment (FESEM – ZEISS Company, Oxford Instruments) connected to the FESEM was used to carry out the elemental analysis of the synthesized NMs. The investigation was carried out with a 10 kV electron beam in plain view mode. For each nanomaterial, the values of Lα and Kα energies were specified. The morphology of the prepared NMs was studied utilising transmission electron microscopy (TEM) with a Tecnai G2 20 S-TWIN [FEI] electron microscope running at 200 kV. The apparatus has a 0.14 nm line resolution, 0.24 nm point resolution, and 1.0 nm STEM resolution. The surface composition of the nanoparticles was examined using X-ray photoelectron spectroscopy (XPS) using a Thermo VG Scientific MULTILAB instrument with AlKα radiation as a monochromator. Employing Shirley-type background and Lorentzian–Gaussian functions, the XPX peaks 41 software deconvoluted the XPS peaks. For electrochemical Mott–Schottky measurement, 0.1 M Na$_2$SO$_4$ electrolytic solution was employed. The data were recorded by a 3 electrode system employing a

Multi Autolab/M$_2$0$_4$ electrochemical workstation (Netherlands, Metrohm Autolab B.V.), where, Ag/AgCl (3 M KCl), platinum wire, and photocatalyst coated over graphite sheet were applied as the reference, counter, and working electrode, respectively. Before the initiation of the electrochemical experiments, Ar gas was purged for 20 min to eliminate oxygen or any other gas adsorbed on the surface of the sample. For the Mott–Schottky analysis, the samples were scanned varying from −1 V to +1 V (*vs.* Ag/AgCl and then transformed to potential *vs.* NHE). The NMs optical absorbance and band gaps were estimated using a UV-visible diffuse reflectance spectrophotometer (UV-Vis DRS; JASCO, Japan). The bandgap energy of the prepared NMs was calculated using Tauc's equation as follows:

$$\alpha h v = A(h v - E_g) \qquad (1)$$

where,

$$E_g(\text{eV}) = \frac{1240}{\lambda_G} \qquad (2)$$

In which A is a constant, E_g represents the band gap energy, v is the photon frequency, and h is the Planck constant. The S factor, equal to 1/2 or 2 for the indirect and direct and transition band gaps, respectively, depends on the kind of electron transfer.[20] A colorimetric method was used to assess residual Cr(VI) concentration as depicted by APHA.[21]

3. Results and discussion

3.1. Nanomaterial characterization

3.1.1. XRD analysis. The XRD analysis of the BiOBr, In$_2$S$_3$, SrGO, and BiOBr–In$_2$S$_3$–SrGO nanocomposites is shown in Fig. 1. Fig. 1(a) demonstrates the XRD spectra of BiOBr. The prominent diffraction peaks at 2θ values of 10.9°, 21.9°, 25.1°, 31.6°, 32.2°, 39.3°, 46.2°, 50.6°, and 57.1° were indexed to the (001), (002), (101), (102), (110), (112), (200), (104), and (212) planes, respectively, indicating the tetragonal phase of BiOBr (JCPDS card number 09-0393). Similar observations were also
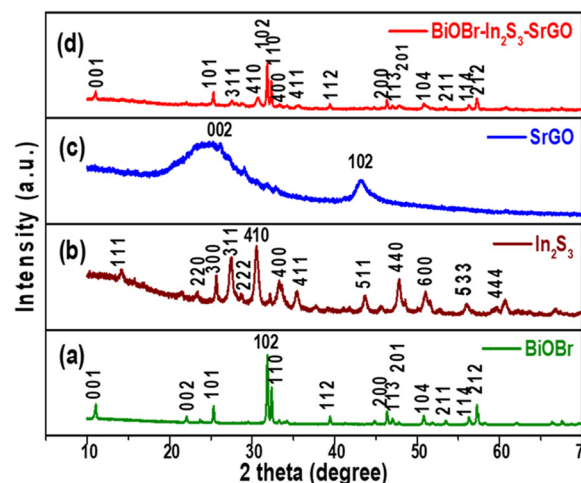

Fig. 1 X-ray diffraction patterns of (a) BiOBr, (b) In$_2$S$_3$, (c) SrGO, and (d) the BiOBr–In$_2$S$_3$–SrGO nanocomposite.

reported in the literature.[22,23] Furthermore, the XRD patterns showed an apparent propensity to grow along the (102) and (110) directions, as shown in Fig. 1(a).[24] Diffraction peaks at 2θ values of $13.9°$, $23.7°$, $25.0°$, $27.5°$, $28.7°$, $31.4°$, $33.3°$, $35.4°$, $43.7°$, $47.9°$, $51.0°$, $56.1°$ and $59.6°$ in Fig. 1(b) were indexed to the (111), (220), (300), (311), (222), (410), (400), (411), (511), (440), (600), (533) and (444) planes, respectively. This observation matches JCPDS card no. JCPDS-32-0456, 05-0722, which assured the cubic structure of In_2S_3.[25,26] Fig. 1(c) shows the XRD spectra of SrGO. The primary diffraction peaks at 2θ values of $26.4°$ and $43.2°$ were indexed to the (002) and (102) planes, respectively. The appearance of a maximum intensity peak at a 2θ value of $\sim 26.4°$, which corresponds to the characteristic (002) reflection, reveals the occurrence of parallel graphene layers in SrGO. The literature has reported a similar observation.[27] In Fig. 1(d), peaks of both BiOBr and In_2S_3 phases can be seen, which indicates the successful formation of the BiOBr–In_2S_3–SrGO nanocomposite. Nevertheless, no clear distinctive peaks of SrGO are seen in the BiOBr–In_2S_3–SrGO nanocomposite; this could be because the S–rGO sheets are not aggregating to the same extent.[28]

The average crystalline sizes and lattice strains of the synthesized NMs were calculated using the Williamson and Hall (W–H) equation as shown in eqn (3).

$$\beta\cos\theta = 4\sin\theta + K\lambda/D, \quad (3)$$

Here, θ stands for the angle of diffraction, FWHM (full width at half maximum), D stands for average crystal size,

K represents the constant with a value of 0.89, and λ denotes wavelength with a value of 0.154 nm. With $4\sin\theta$ on the X-axis and $\cos\theta$ on the Y-axis, a plot is therefore created. The average crystalline size is represented by the Y-intercept, whereas the slope of the curve indicates lattice strain. In this work, the average crystalline size of the BiOBr, In_2S_3, SrGO, and BiOBr–In_2S_3–SrGO nanocomposites is 0.02 nm, 0.188 nm, 2.39 nm, and 0.017 nm, respectively.

3.1.2. FTIR Analysis. Fig. 2 displays the FTIR spectra of pure BiOBr, In_2S_3, SrGO, and BiOBr–In_2S_3–SrGO nanocomposites. As seen in Fig. 2(a), the appearance of a peak below 1000 cm^{-1} designates the existence of Bi–O bonds, whereas the Bi–Br band appears at absorption peaks between 1000 and 1500 cm^{-1}. The peak centered at 1613 cm^{-1} represents the flexural vibration mode of O–H in free water molecules.[29] Fig. 2(b) shows the FTIR spectra of In_2S_3. The peak at 1600 cm^{-1} corresponds to the C=O stretching vibration of the atmospheric CO_2 absorbed in the sample.[30] The peaks from 3200 to 3750 cm^{-1} show a vibrational stretching mode of the OH group, which can be attributed to water absorption on the sample.[31] Prominent absorption bands at around 1300 to 1600 cm^{-1} and 574 cm^{-1} could be attributed to In–S, which is consistent with the XRD patterns.[32] FTIR spectra of SrGO are displayed in Fig. 2(c). The O=C=O starching revealing the occurrence of oxygen in the S–rGO specimen is demonstrated by the strong peak at 2359.48, and the C=C stretching vibration is indicated by the peak at 1697.05. The occurrence of the OH group is shown by the peaks at 3564.77 and 3819.33.[15,33] Fig. 2(d)
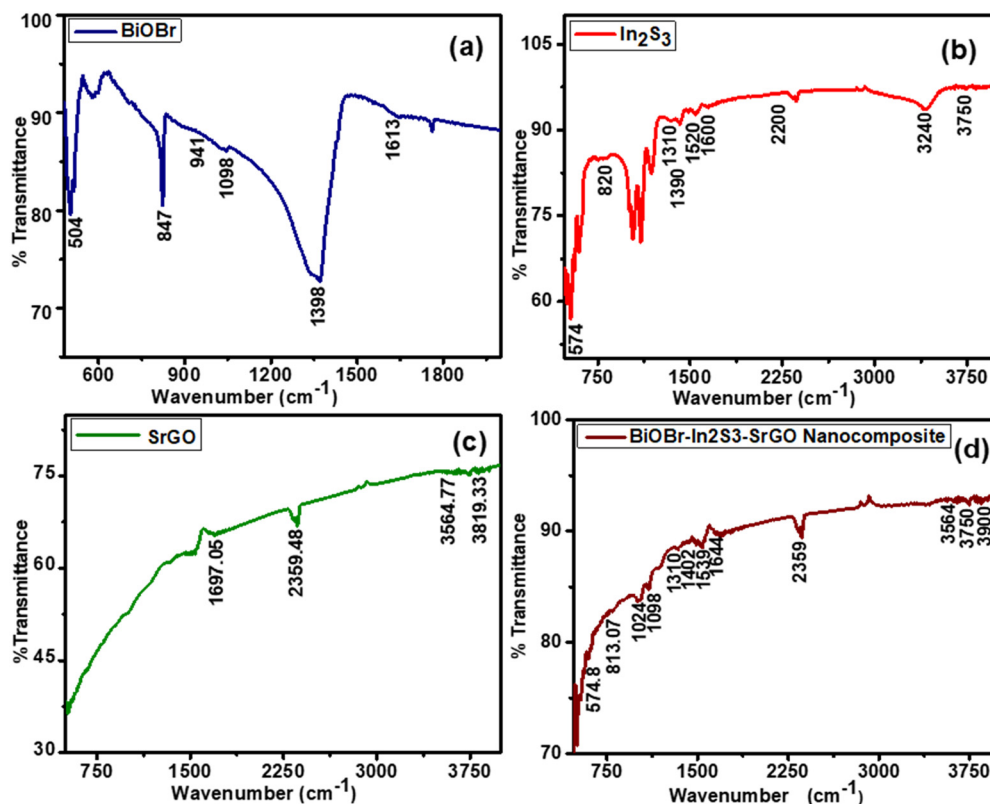

Fig. 2 FTIR spectra of the synthesized NMs (a) BiOBr, (b) In_2S_3, (c) SrGO, and (d) the BiOBr–In_2S_3–SrGO nanocomposite.

illustrates the FTIR spectra of the BiOBr–In$_2$S$_3$–SrGO nanocomposites. The absorption peaks at 574.8 and 813.07 cm^{-1} of the nanocomposite are ascribed to the Bi–O bonds, whereas those between 1000 and 1500 cm^{-1} are attributed to the Bi–Br band. Similarly, the peaks between 3200–3700 cm^{-1} and 1644 cm^{-1} are caused by the O–H stretch vibration of water and the C=O stretching vibration of carbon dioxide, absorbed on the nanocomposite, respectively. In addition, a prominent peak at 2359 cm^{-1} (O=C=O stretching) is due to the occurrence of oxygen in the SrGO. These results have authenticated that the BiOBr–In$_2$S$_3$–SrGO hetero-structure has been successfully prepared.

3.1.3. Raman analysis. Raman spectroscopy investigation is used to determine the structure and defects of NMs. Fig. 3(a) represents the Raman spectra of BiOBr NMs. There are 2 A$_{1g}$, B$_{1g}$, and E$_g$ Raman active modes, as shown in Fig. 3(a). The bands for BiOBr are designated to the A$_{1g}$ internal Bi–Br stretching mode at 57.0, 91.7, and 112.1 cm^{-1}. The E$_{1g}$ Bi–Br stretching mode is attributed to the band at 160.7 cm^{-1}.[34] The firm peaks confirm the excellent crystallinity structure of the BiOBr NMs. Fig. 3(b) illustrates the Raman spectrum of In$_2$S$_3$ NMs. From Fig. 3 (b), distinct Raman peaks are observed at about 274, 309, and 369 cm^{-1}. The A$_{1g}$ mode can be attributed to the highly polarized Raman peak at 369 cm^{-1}, the F$_{2g}$ mode at 309 cm^{-1}, and the E$_g$ mode at 274 cm^{-1}.[35] These Raman peaks show a strong correlation with the previously reported In$_2$S$_3$ NMs' active mode in the cubic phase.[36,37] Fig. 3(c) illustrates the Raman spectra of SrGO. As seen in

Fig. 3(c), all of the peaks show a slight red shift (bands appeared at 1351 and 1588 cm^{-1}) and narrowed, which might be due to the reorganization of the structure during the reduction and sulfonation process. When comparing SrGO (2.12) to pure GO, a slight drop in the ID/IG ratio was observed. This suggests that during SrGO's reduction and sulfonation processes, a small number of sp^3 defects associated to the oxygenation groups were diminished.[38,39] Fig. 3(d) shows the Raman spectra of the nanocomposite (BiOBr–In$_2$S$_3$–SrGO). The peaks at 57.02, 69.67, 91.7, 112.1, 160.7, 222.5, and 267.5 cm^{-1} represent the Raman spectra of the nanocomposite. The bands at 57.02, 69.67, 91.7, and 112.1 cm^{-1} are designated to the A$_{1g}$ internal Bi–Br stretching mode. The band at 160.7 cm^{-1} is attributed to the E$_{1g}$ Bi–Br stretching mode. The appearance of a peak at about 267.5 cm^{-1} represents the in-plane E$_g$ vibration mode of In$_2$S$_3$. The above peaks indicate the cubit structure of the BiOBr–In$_2$S$_3$–SrGO nanocomposite. In summary, the findings of the Raman analysis on the structure of BiOBr, In$_2$S$_3$, and the BiOBr–In$_2$S$_3$–SrGO nanocomposite corroborate with the findings of the XRD study.

3.1.4. PL spectra analysis. The recombination rate of the photoinduced charge carrier can be predicted using the photoluminescence spectral analysis. Lower photoluminescence intensity denotes a minimum recombination rate of photoexcited electron and hole pairs. Whereas greater photoluminescence intensity indicates a high recombination rate of photogenerated charge.[15] Fig. 4(a) shows the photoluminescence emission spectra of the BiOBr, In$_2$S$_3$, SrGO, and BiOBr–In$_2$S$_3$–SrGO nanocomposite.
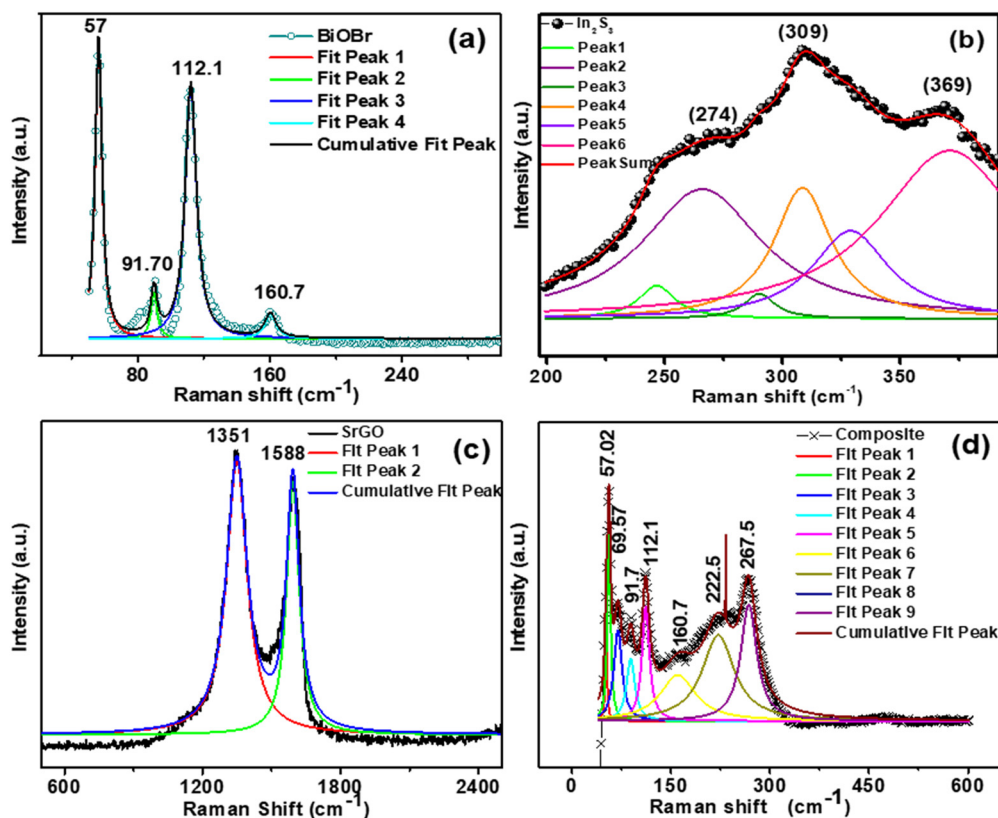

Fig. 3 Raman shift *versus* intensity of the synthesized NMs (a) BiOBr, (b) In$_2$S$_3$, (c) SrGO, and (d) the BiOBr–In$_2$S$_3$–SrGO nanocomposite.

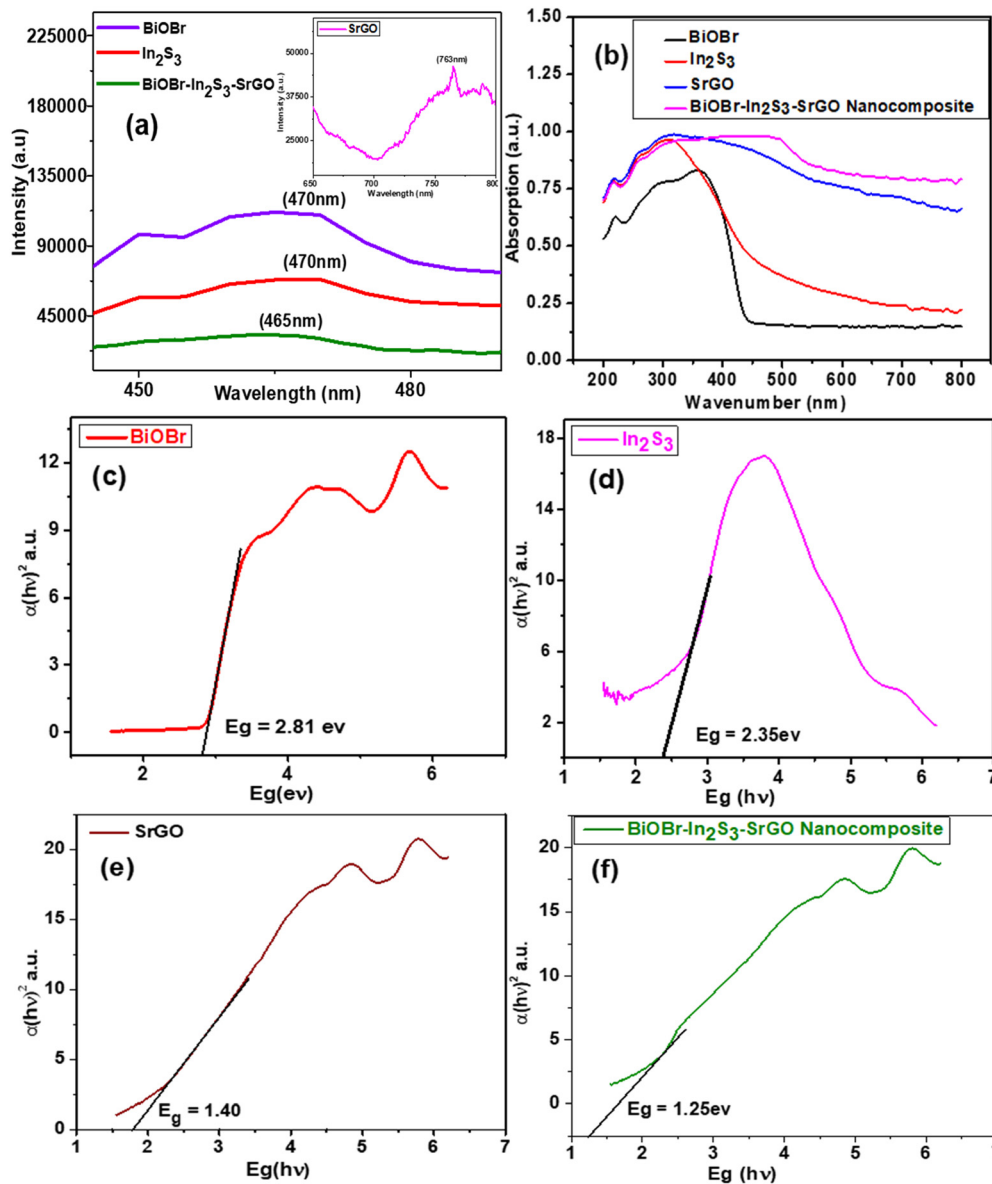Fig. 4   (a) Photoluminescence (PL) spectra of BiOBr, In₂S₃, SrGO and the BiOBr–In₂S₃–SrGO nanocomposite, (b) UV-DRS spectra of the synthesized NMs, and Willliamson-hall plots of (c) BiOBr, (d) In₂S₃, (e) SrGO, and (f) the BiOBr–In₂S₃–SrGO nanocomposite.

The PL spectra of BiOBr, In₂S₃, and BiOBr–In₂S₃–SrGO NMs were obtained in the 400–600 nm emission peak range. The bare BiOBr and In₂S₃ have the highest emission peak, centered at 470 nm.[40–42] PL spectra of SrGO were obtained in the emission peak range of 650 to 800 nm, and the emission peak centered at 763 nm, which is in good agreement with the reported literature.[43] On the other hand, the composite has the lowest emission peak at 465 nm. It is evident from the figure that the photoluminescence intensity of these NMs diminishes and reaches its lowest value in the synthesized nanocomposite. This phenomenon indicated that the recombination rate of photoinduced charge carriers significantly decreases in the nanocomposite. This observation is likely due to the formation of the Z-scheme heterostructure between the BiOBr and In₂S₃ that improves the efficiency of photoinduced charge transfer with high redox ability.[44]

3.1.5. UV DRS analysis. In general, the light absorption property heavily relies on the band structure of the semiconductor materials, severely constraining the photocatalytic activity. Thus, UV-VIS DRS was used to compute the light absorption characteristic of NMs.[45] Fig. 4(b) shows the bathochromic shift of the BiOBr–In₂S₃–SrGO nanocomposite with respect to the individual NMs. The edges of In₂S₃, SrGO, BiOBr, and BiOBr–In₂S₃–SrGO have been redshifted (bathochromic shift) to 311.5 nm, 319.5 nm, 359 nm, and 462 nm, respectively, showing that the formation of the nanocomposite improves the responsiveness to visible light. The band gaps of the produced nanocomposite were determined using Tauc plots, as shown in Fig. 4(c). The computed band gap energy (E_g) of BiOBr is 2.81 eV, which is well supported by many documents in the literature.[46,47] The calculated E_g value of In₂S₃ is 2.35 eV, as

shown in Fig. 4(d), which is well correlated by many reports in the literature.[48,49] Fig. 4(e) shows the E_g value of SrGO, which increased slowly from 0.95 eV to 1.37 eV, implying that the chemical modification of rGO with sulphate groups changed its optical characteristics, almost identical to the reported literature.[50] The calculated E_g value of the BiOBr–In$_2$S$_3$–SrGO nanocomposite is 1.25 eV, as shown in Fig. 4(f). As can be seen from Fig. 4(f), BiOBr has a slightly low bandgap energy of 2.81 eV, which suggests that it has moderately visible light absorption efficiency. After forming the nanocomposite, the E_g value was further reduced to 1.25 eV, and thus, the visible light harvesting ability was effectively increased. This shows the unique and productive interaction among the BiOBr, In$_2$S$_3$, and SrGO in the nanocomposite.

3.1.6. FESEM micrographs. FE-SEM analysis was carried out to observe the morphological features, distribution and size of the prepared NMs. Fig. 5(a) shows a clear, heterogeneous, rectangular 3D nanoplatelet structure of BiOBr with an average scale of 200 nm. The formation of a nanoplatelet structure offers a high surface area and improves the visible light absorption ability. Further formation of the nanoplatelet geometry with a high surface area enhances the contact area with SrGO, facilitating the photogenerated charge transfer efficiency and increasing the photocatalytic properties. A similar sheet-shaped structure with a clear and smooth surface of BiOBr NMs has been documented in the literature.[51] Fig. 5(b) shows the FE-SEM image of In$_2$S$_3$ NMs. The FE-SEM image reveals a homogeneously distributed spherical and granular structure of In$_2$S$_3$ with an average scale of 300–400 nm.[52] It is seen that the particles are dense without pinholes.[53] The FESEM image of SrGO is demonstrated in Fig. 5(c), which reveals that the SrGO surface displayed an interconnected 3D porous, corrugated, and exfoliated structure. The conversion of GO to rGO is accountable for this corrugated configuration. Further removal of oxygen-carrying groups from the GO surface while converting to rGO induces the formation of aggregated structures. The π–π

stacking phenomena of GO most likely causes the formation of this aggregated structure.[15] Fig. 5(d) shows the high dispersion and uniformity of the individual constituents of the BiOBr–In$_2$S$_3$–SrGO nanocomposite. It is evident from Fig. 5(d) that a bunch of uniformly distributed rectangular 3D nanoplatelets of BiOBr and dense nanospheres of In$_2$S$_3$ anchored on the corrugated, exfoliated, and 3D porous interconnected configuration of S–rGO.

3.1.7. EDAX spectra analysis. The elemental compositions of BiOBr, In$_2$S$_3$, SrGO, and the BiOBr–In$_2$S$_3$–SrGO nanocomposite were analyzed using EDAX spectroscopy. Fig. 6(a) demonstrates the EDAX spectrum for the BiOBr, which revealed the occurrence of a stoichiometric ratio of Bi, O, and Br in the NMs. Based on the EDAX peaks, the amounts of O$_2$, Bi, and Br present in the BiOBr NMs are 51.8, 30.4, and 17.8%, respectively. Fig. 6(b) displays the EDAX spectra of the synthesized In$_2$S$_3$ NMs. The In$_2$S$_3$ is composed of indium at 90.1 weight%, which is larger than sulfur at 9.9 weight%. The existence of a stoichiometric ratio of In and S elements confirmed that the In$_2$S$_3$ NMs were well synthesized. In Fig. 6(c), the EDAX data of SrGO confirm the occurrence of carbon (C), oxygen (O) and sulphur elements in the NMs. According to the EDAX spectra, the quantity of C in S–rGO is 81.9 weight%, much more than O, which is 17 weight%. As sulfur was applied as a doping agent only, the existence of S in the compound is very small, which is 1.1 weight%. Fig. 6(d) exhibits the EDAX spectra of the synthesized BiOBr–In$_2$S$_3$–SrGO nanocomposite. Fig. 6(d) confirms the presence of Bi, O, Br, In, S, and C in the BiOBr–In$_2$S$_3$–SrGO nanocomposite. The nanocomposite has a larger weight percentage of carbon (46.4), bismuth (18.1), and indium (15) compared to other elements present in it.

3.1.8. HRTEM micrographs. The heterostructure of the BiOBr–In$_2$S$_3$–SrGO ternary nanocomposite was investigated by HRTEM through morphological study. As shown in Fig. 7(a), In$_2$S$_3$ was found to consist of a spherical structure with average sizes of 50 nm, whereas BiOBr was a 3D-nanoplatelet structure with an irregular size and shape of average 400 nm, both of which were decorated on the surface of sheet-like SrGO. The HRTEM image that corresponded to the selected area in the inset of Fig. 7(a) displayed lattice fringes with spacings of 0.324 and 0.284 nm. These fringes could be attributed to the In$_2$S$_3$ crystal plane (311), and the BiOBr crystal plane (102) respectively.[54] This aligns well with the XRD results.

3.1.9. Mott–Schottky plot analysis. In order to ascertain the variations in the electrical characteristics of the BiOBr photocatalyst, Mott–Schottky (MS) measurements were executed by means of the impedance technique.[55] Fig. 7(b) shows the M-S curves of the n-type characteristics of BiOBr and In$_2$S$_3$, respectively, due to the positive slope.[56] The flat potentials of BiOBr and In$_2$S$_3$ are measured to be −0.30 V and −0.95 V (vs. SCE), which are −0.06 V and −0.71 V (vs. NHE). Furthermore, the slope of In$_2$S$_3$ was significantly smaller compared to BiOBr, revealing the generation of more electrons in the In$_2$S$_3$ and therefore comprising a higher charge density for efficient Cr(VI) reduction in the Z-scheme photocatalyst.[57] Since the conduction band energy (E_{CB})
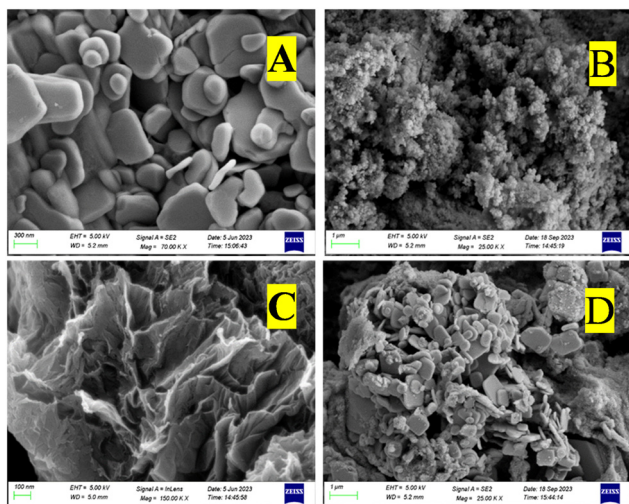

Fig. 5 FE-SEM micrographs of (a) BiOBr, (b) In$_2$S$_3$, (c) SrGO, and (d) the BiOBr–In$_2$S$_3$–SrGO nanocomposite.
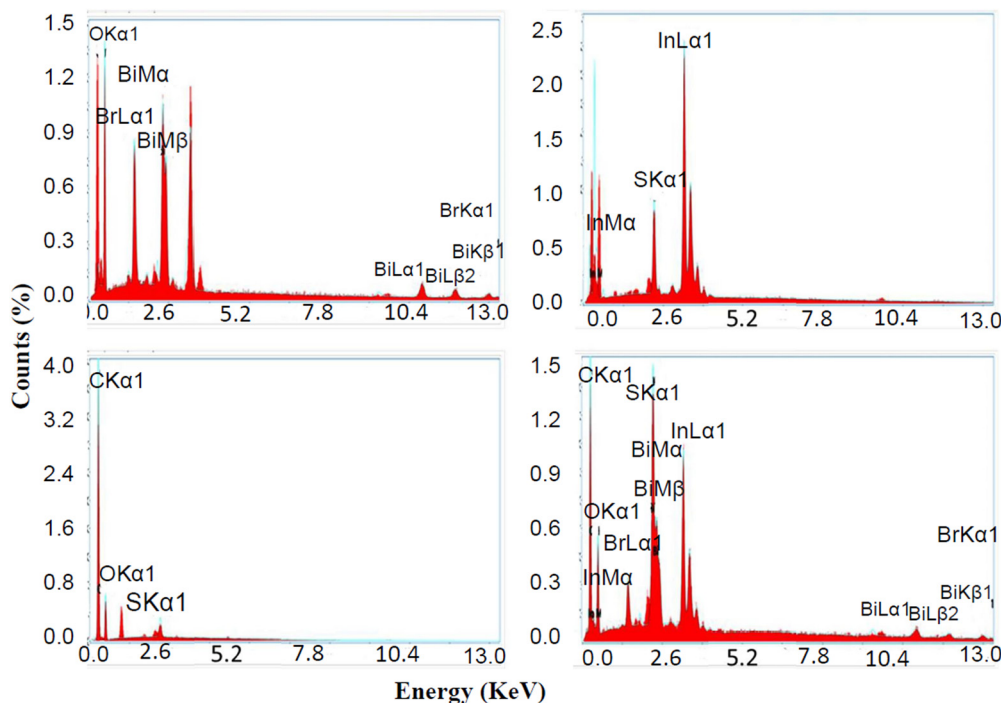
Fig. 6   Energy dispersive X-rays spectrum (EDX) of (a) BiOBr, (b) In_2S_3, (c) SrGO, and (d) the BiOBr–In_2S_3–SrGO nanocomposite.
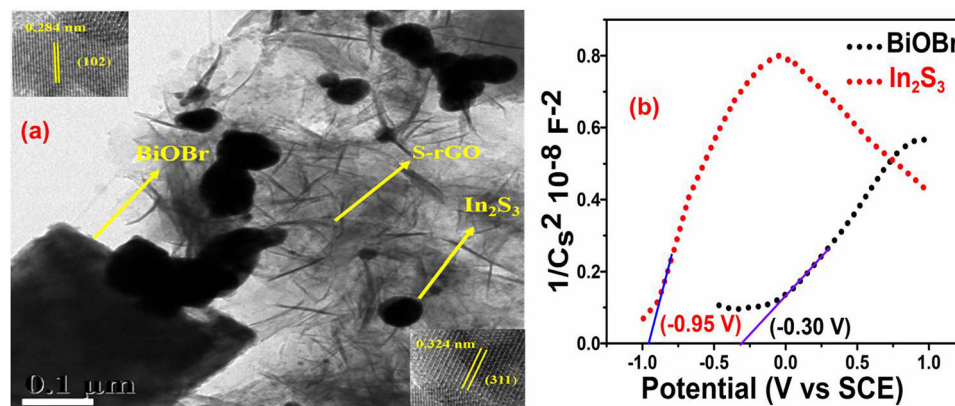

Fig. 7   (a) TEM image of the BiOBr–In_2S_3–SrGO ternary nanocomposite (Inset: HRTEM image of BiOBr–In_2S_3–SrGO ternary nanocomposite). (b) Mott–Schottky plot of BiOBr and In_2S_3 nanomaterials.

position is about 0.10 V above the flat-band potential, in the present study the E_{CB} positions of BiOBr and In_2S_3 were calculated at about −0.16 V and −0.81 V, respectively, which is well supported with the reported literature.[58,59] By deducting E_g (bandgap energy) from the position of the CB minimum, one can determine the VB maximum position[60] and thus, in the present study, the calculated VB of BiOBr and In_2S_3 are 2.65 V and 1.54 V, respectively.

3.1.10.   XPS analysis. XPS measurements were carried out to examine the valence states and chemical composition of several components in the BiOBr–In_2S_3–SrGO ternary nanocomposite (Fig. 8). As shown in Fig. 8(a), bare In_2S_3 shows two distinct peaks located at 445.3 and 453.1 eV that were

attributed to In $3d_{5/2}$ and $3d_{3/2}$ of In^{3+}, respectively.[61] Furthermore, the Bi 4f spectrum of bare BiOBr in Fig. 8(b) shows characteristic peaks Bi $4f_{7/2}$ and $4f_{5/2}$ appearing at a binding energy of 158.6 and 163.5 eV that were assigned to Bi^{3+}, respectively.[62] Similarly, the binding energies of 468.6 and 469.8 eV in bare BiOBr in Fig. 8(c) correspond to characteristic peaks of Br 3d (Br $3d_{5/2}$ and Br $3d_{3/2}$).[63] In contrast, when comparing the BiOBr–In_2S_3–SrGO ternary nanocomposite in Fig. 8(a–c) to bare samples, the In 3d states shifted to higher energies, whereas the Bi 4f and Br 3d states shifted to lower energies. Fig. 8(d) demonstrates the high resolution S 2p spectra of bare In_2S_3. The two fitted peaks at 162.2 and 164.2 eV were attributed to S($2p_{3/2}$) and S ($2p_{1/2}$) of bare In_2S_3,
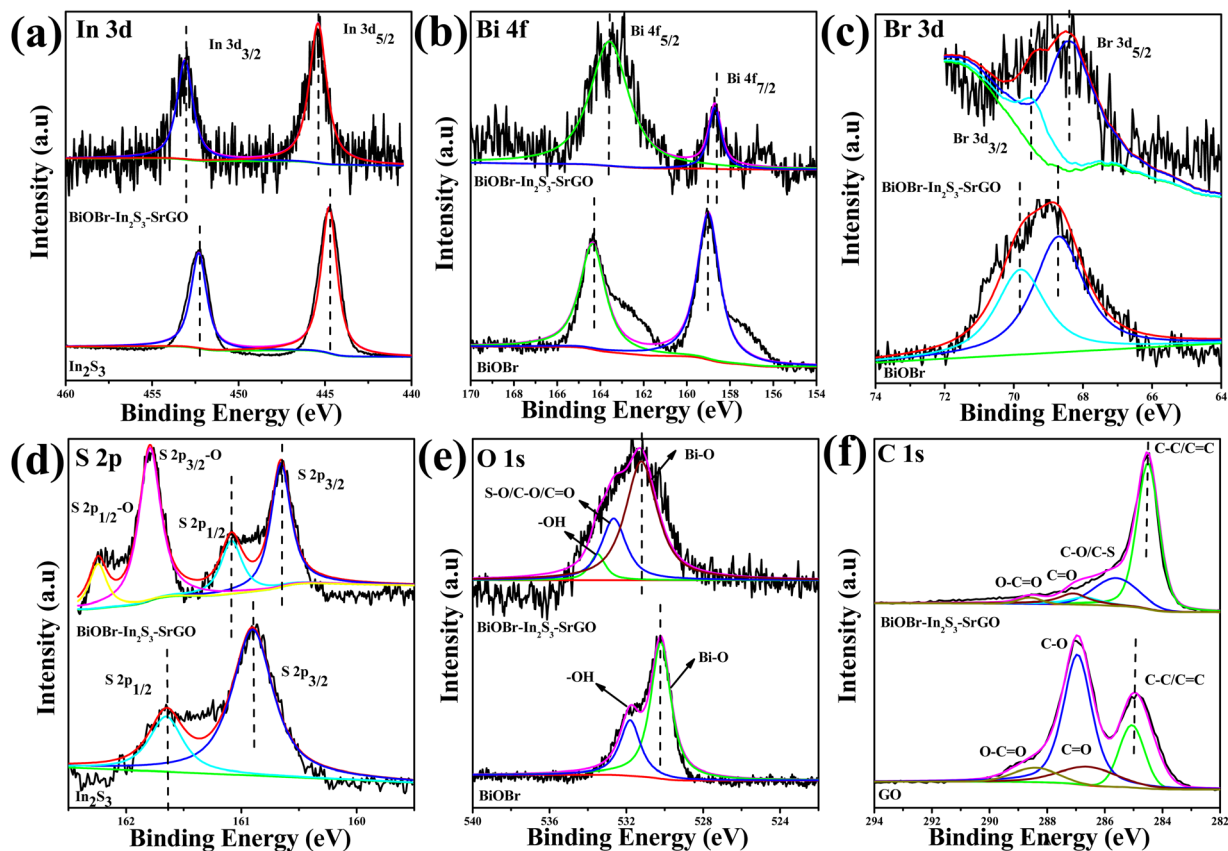
Fig. 8 High-resolution XPS spectra of (a) In 3d, (b) Bi 4f, (c) Br 3d, (d) S 2p, (e) O 1s, and (f) C1s from the bare In_2S_3, BiOBr and BiOBr–In_2S_3–SrGO ternary nanocomposites.

respectively.[61] On the other hand, the two S 2p peaks of the BiOBr–In_2S_3–SrGO ternary nanocomposite were shifted to a higher binding energy of 161.4 and 160.2 eV, respectively, and two more doublet peaks were observed at 164.7 and 163.1 eV, respectively. These were ascribed to the S 2p 3/2 and 1/2 peaks of the S–O bonds, which is well supported with the reported literature.[64] Two peaks, representing Bi–O (530.2 eV) and –OH (531.8 eV), respectively, were seen in the fitted O 1s spectra of BiOBr in Fig. 8(e).[65] However, the BiOBr–In_2S_3–SrGO ternary nanocomposite shows a new peak at 531.6 eV; however, it may be attributed to the S–O/C–O/C=O bonds in S–rGO.[66,67] In Fig. 8(f), the deconvoluted C 1s core level spectrum of the BiOBr–In_2S_3–SrGO ternary nanocomposite reveals four distinct peaks at 284.4, 285.7, 287.1, and 288.6 eV, which are attributed to C–C/C=C, C–O/C–S, C=O, and O–C=O, respectively.[68] In comparison with the C 1s core level spectrum of GO, the prominent peaks at C=C and the minor peaks at O–C=O indicate that the GO was effectively reduced during the synthesis process, confirming the presence of reduced graphene oxide (rGO) in the BiOBr–In_2S_3–SrGO ternary nanocomposite. Additionally, the peak at 285.7 eV (C–O/C–S) demonstrated that the sulfur ion in the BiOBr–In_2S_3–SrGO ternary nanocomposite was doped in the carbon lattice to create SrGO rather than physically adsorbed on the graphene sheets. Taking everything into account, it was evident

that, as seen in Fig. 8(a–f), each element's binding energy state in the BiOBr–In_2S_3–SrGO ternary nanocomposite had shifted somewhat when compared to the pure samples. This suggested that photo-excited electrons were moving from BiOBr to In_2S_3 in the heterostructure through the S-doped rGO.[54,69] Because the VB of In_2S_3 is larger compared to BiOBr and due to the outstanding electrical conductivity and storage ability of S–rGO, the S–rGO can offer interfaces for photoinduced electrons in the CB of BiOBr to combine with the holes of the VB of In_2S_3 in the composite photocatalysts, which may improve the hole–electron pair separation efficiency. Therefore, a Z-scheme model might describe the charge transfer pattern in this study.

3.2. Cr(vi) removal profile of the BiOBr–In_2S_3–SrGO nanocomposite

The Cr(vi) removal profile under dark and visible light illumination conditions is shown in Fig. 9(a). From the figure, it can be seen that when the heterojunction was kept under dark conditions for 120 min, it exhibits no noteworthy Cr(vi) removal (22%) at an initial 100 mg L^{-1} Cr(vi). Upon visible light illumination for 120 min, Cr(vi) removal was increased to 96.6%. When exposed to visible light, the individual NMs of BiOBr and In_2S_3 had the lowest photo-reduction activity of 30.9 and 33.4%, respectively. On the other hand, the photo-reduction of Cr(vi) is considerably enhanced to 96.6% using

the BiOBr–In$_2$S$_3$–SrGO nanocomposite. Table 1 provides a comparative analysis of different photocatalytic systems reported in the literature for Cr(vi) reduction under visible light illumination. Compared to literature reports, the BiOBr–In$_2$S$_3$–SrGO nanocomposite distinctively exhibits superior Cr(vi) reduction activity compared to all other catalysts, as shown in Table 1. The improved photocatalytic activity of the nanocomposite might be due to bathochromic shift and narrowing of the bandgap energy with respect to the individual NMs, as discussed earlier in the UV-DRS analysis shown in Fig. 4(c–f). This is also well supported by the lower photoluminescence intensity of the nanocomposite than individual NMs, as shown in Fig. 4(a). This result suggests that the recombination rate of photogenerated charge carriers is inhibited, which in turn increases the activity of photocatalytic Cr(vi) reduction. The photocatalytic reduction of Cr(vi) was improved further by the addition of S-doped rGO in the nanocomposite because it enhanced the surface area, encouraged nucleation, and provided anchor sites for interfacial contact between BiOBr and In$_2$S$_3$. Thus, the efficiency of electron flow increases, particularly at the interface, which is further accelerated by delocalized π electrons in the sp^2 carbon of rGO.[15,16] Additionally, S doped r-GO prevents the rate of photo-excited charge carrier recombination. Fig. 9(b) shows the Cr(vi) reduction profile of the BiOBr–

In$_2$S$_3$–SrGO nanocomposite at varying initial Cr(vi) doses. The solutions having 25 mg L^{-1} and 50 mg L^{-1} initial Cr(vi) doses exhibit 100% reduction within 30 and 60 min, respectively. Meanwhile, 96.6% of the Cr(vi) reduction was achieved by the nanocomposite at 100 mg L^{-1} of the initial Cr(vi) dose within 120 min. Whereas, Fig. 9b.1 shows the comparison between the reduction efficiency of the BiOBr–In$_2$S$_3$–SrGO nanocomposite under dark and visible light conditions at 100 mg L^{-1} initial Cr concentration. When the heterojunction was rendered to dark reaction for 120 min, it revealed no substantial Cr(vi) reduction, *i.e.*, about 22% removal at an initial 100 mg L^{-1} Cr(vi), which was taken as a control. But when irradiated with visible light for 120 min, Cr(vi) removal was boosted, *i.e.*, up to 96.6%.

3.3. Reduction profile of chromium at different pH

The Cr(vi) reduction experiment by the nanocomposite was conducted with different pHs of 2, 4, 6, and 8 at 100 mg L^{-1} initial Cr(vi) concentration and achieved almost 96.6%, 85.3%, 53%, and 47% removal, respectively. In this study, using a BiOBr–In$_2$S$_3$ Z-scheme heterojunction, the Cr(vi) elimination efficacy was 96.6% at pH 2, while at pH 8, it was only 47% under illumination of visible light within 120 min. Typically, Cr$_2$O$_7^{2-}$ is the primary component under acidic conditions, while CrO$_4^{2-}$ in alkaline conditions.[79] In an acidic environment,
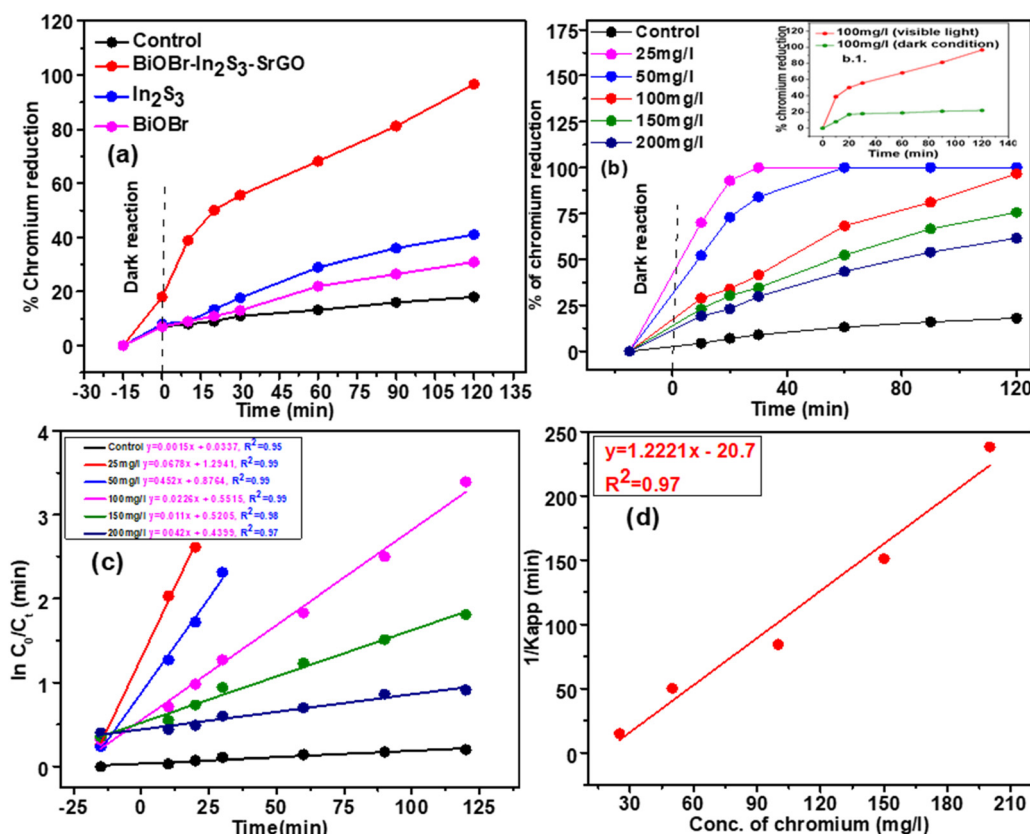

Fig. 9 (a) Demonstration of the Cr(vi) removal profiles by different individual nanomaterials and the nanocomposite at an initial dose of 100 mg L^{-1}. (b) Cr(vi) removal profiles by the nanocomposite at varying initial Cr(vi) doses (b.1) Cr(vi) removal profiles by the nanocomposite under visible light and dark conditions. (c) Pseudo first order Cr(vi) removal kinetics at varying doses of Cr(vi). (d) Variation of the reciprocal of apparent rate constant profile at varying initial Cr(vi) dose.

Table 1 Comparative analysis of the BiOBr–In$_2$S$_3$–SrGO nanocomposite's Cr(VI) removal performance with that of other catalysts documented in the literature

Sl. no.	Photocatalyst	Synthesis method	Experimental condition	Initial pollutant conc. (mg L^{-1})	Cr(VI) reduction efficiency	Ref.
1	MgCr$_2$O$_4$/WO$_3$	Sol–gel process	Visible light	30	100% in 120 min	70
2	Cu$_2$O/g-C$_3$N$_4$	*In situ* wet chemistry	Visible light	20	77.7% in 120 min	71
3	NiFe$_2$O$_4$/MOF-808	Mechanochemical	Visible light	20	100% in 60 min	72
4	MnFe$_2$O$_4$ and UiO-66-NH$_2$	Solvothermal	Visible light	10	100% in 75 min	73
5	BiVO$_4$/rGO	Hydrothermal	Visible light	10	97.6% in 30 min	74
6	FeVO$_4$/Bi$_4$O$_5$Br$_2$/BiOBr	One-step microwave irradiation	Visible light	30	72.3% in 120 min at PH = 6	75
7	BiVO$_4$/FeVO$_4$@rGO	Hydrothermal	Visible light	20	90.9% in 90 min	76
8	rGO-Sm$_2$MoO$_6$-TiO$_2$	Hydrothermal	Visible light	10	96% in 70 min	77
9	ZnO-Bi$_2$S$_3$	Solvothermal	Visible light	20	95% in 120 min	78
10	BiOBr–In$_2$S$_3$–SrGO	Hydrothermal	Visible light	100	96.6% in 120 min	This work

the photocatalyst surface was likely positively charged by the H$^+$ ion, which aided in photoelectron migration and enhanced the photocatalytic reduction of Cr$_2$O$_7$$^{2-}$ to less hazardous 2Cr(III), as shown in eqn (4).[80] Additionally, the conversion of Cr(VI) to Cr(III) may be facilitated by the high redox potential of Cr$_2$O$_7$$^{2-}$ at very acidic environments.

$$14H^+ + Cr_2O_7^{2-} + 6e^- \rightarrow 2Cr(III) + 7H_2O(acid) \qquad (4)$$
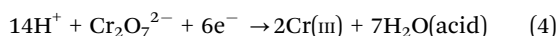
Moreover, the zeta potential of the NMs is increased at lower pH values, which also lessens the repulsive force of the NMs against Cr$_2$O$_7$$^{2-}$ and boosts the Cr(VI) elimination rate. Despite rGO having fewer hydroxyl (OH) and carboxyl (COOH) functional groups than GO at low pH, these functional groups were protonated to be positively charged and captured negatively charged Cr(VI) ions (HCrO$_4$$^-$) *via* electrostatic attraction, leading to a comparatively high Cr(VI) adsorption.[81] Because the Cr(VI) ions adsorbed on GO could readily absorb photoinduced electrons, the photoreduction rate of Cr(VI) increases with the number of Cr(VI) ions adsorbed on GO. Conversely, as the pH increases, the OH and COOH groups on GO deprotonated to exhibit a significant quantity of negative charge, thus causing substantial electrostatic repulsion between Cr(VI) ions (CrO$_4$$^{2-}$) and the rGO, which decreased the Cr(VI) adsorption.[81] Nevertheless, Cr(VI) ions occurred in the form of chromate (CrO$_4$$^{2-}$), under alkaline environments, whose reduction products readily converted to Cr(OH)$_3$ and precipitated, as shown in eqn (5).

$$CrO_4^{2-} + 4H_2O + 3e^- \rightarrow Cr(OH)_3 + 5OH^-(base) \qquad (5)$$
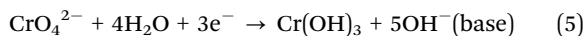
This further weakened the photocatalytic reduction efficiency.[80] As a result, the removal efficiency clearly declined at higher pH.

3.4. Kinetics of Cr(VI) removal using the BiOBr–In$_2$S$_3$–SrGO nanocomposite

The photocatalytic process at liquid–solid interfaces can be efficiently assessed by employing the Langmuir–Hinshelwood kinetic model (LR model) as shown below:

$$r = -\frac{dc}{dt} = \frac{CKk_r}{1 + KC} \qquad (6)$$

where K stands for the LR adsorption equilibrium constant (l mg^{-1}), and r ($-dC/dt$) represents the rate of Cr(VI) reduction [mg L^{-1} min^{-1}]. The t stands for the period of light

illumination in min. The photocatalytic reduction rate constant is denoted by k_r (mg L^{-1}.min), and C is the dose of Cr(VI) (mg L^{-1}). Eqn (6) can be simplified as follows by integrating it at the Cr(VI) dose (C_t) and light irradiation period t.

$$t = \left(\frac{1}{Kk_r}\right) \ln\left(\frac{C_0}{C_t}\right) + (C_0 - C_t)/k_r \qquad (7)$$

where, the starting and equilibrium dose of Cr(VI) at time t is represented by C_0 and C_t, respectively. When the values of C_0 are very small, K_c can be ignored, the above eqn (7) can be simplified as follows:

$$\ln\left(\frac{C_0}{C_t}\right) = k_r K t = K_{app} t \qquad (8)$$

where the apparent first-order rate constant for Cr(VI) reduction is denoted by K_{app} (1/min). The pseudo-first-order kinetics curve for the photoreduction of Cr(VI) by the nano catalyst is depicted in Fig. 9(c). The slope of the plot between ln C_0/C_t *vs.* t (time) was used to determine the rate constant (K_{app}). The LR kinetic model can be further simplified as shown below.[82]

$$\frac{1}{K_{app}} = \frac{1}{k_r K} + \frac{C_0}{k_r} \qquad (9)$$

Fig. 9(d) displays the plot of $1/K_{app}$ against the initial Cr(VI) concentration (C_0). The higher correlation coefficient value ($R^2 = 0.97$) indicates that the experimental data is well-fitted with this LH model. The intercept and slope of the straight line shown in Fig. 9(c) are used to estimate the values of the photocatalysis rate constant (k_r) and Langmuir–Hinshelwood adsorption equilibrium constant (K). In this work, the k_r and K values are determined to be 0.818 min^{-1} and -0.059 mg L^{-1}, respectively. This shows that the rate of adsorption by the nanocomposite is zero, while the rate of Cr(VI) reduction is very high.

3.5. Regeneration and recycling of the BiOBr–In$_2$S$_3$–SrGO nanocomposite

The regeneration and recycling capacities of the BiOBr–In$_2$S$_3$–SrGO nanocomposite were tested, as reported in the literature.[83] Following the photocatalytic reaction, the BiOBr–In$_2$S$_3$–SrGO nanocomposite was immersed in a 10% HNO$_3$ solution for 1 h. It was then repeatedly rinsed with deionized
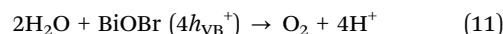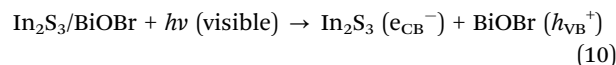
water and dried in a vacuum oven. The reborn BiOBr–In$_2$S$_3$–SrGO nanocomposite was re-examined for its Cr(VI) removal ability using a fresh Cr(VI) solution in the identical experimental setup as discussed earlier. The Cr(VI) removal efficiencies in the 1st, 2nd, and 3rd cycles were 96%, 87%, and 81%, respectively, at an initial dose of 100 mg L^{-1}. This finding indicates that recycling the BiOBr–In$_2$S$_3$–SrGO catalyst is both convenient and cost-effective.

3.6. Mechanism of Cr(VI) removal using the BiOBr–In$_2$S$_3$–S–rGO nanocomposite

Upon visible light irradiation, the electrons exited from the VB to their respective CB of both In$_2$S$_3$ and BiOBr, forming a hole in the VB. The work functions of BiOBr, SrGO, and In$_2$S$_3$ are 6.25 eV,[84] 5.1 eV,[85] and 3.95 eV[86] respectively. The Fermi level of a semiconductor can be estimated using the following formula: $E_f = E_{vac.} - W_f$, where, E_f: represents the Fermi level, E_{vac} stands for the vacuum level, and W_f: denotes the work function.[84,87,88] Generally, the Fermi level is more negative the greater the work function.[89–93] Hence, the Fermi level of BiOBr is more negative compared to SrGO. Similarly, the Fermi level of SrGO is more negative compared to In$_2$S$_3$. So, the photo-induced electrons from the CB of BiOBr can straightforwardly migrate to the S–rGO NMs through the Schottky barrier. In the meantime, the electron from S-doped rGO NMs also transfers to the VB of In$_2$S$_3$, due to the more negative Fermi energy of S–rGO compared to the VB level of In$_2$S$_3$. Furthermore, in the present study, this observation has been validated by Mott–Schottky analysis. Applying Mott–Schottky analysis, the E_{CB} positions of BiOBr and In$_2$S$_3$ were calculated at −0.16 V and −0.81 V, respectively. Similarly, E_{VB} positions of BiOBr and In$_2$S$_3$ were calculated at about 2.65 V and 1.54 V, respectively. This observation clearly indicated that the movement of the e$^-$ follows the Z-scheme pattern from the CB of BiOBr (−0.16 V) towards S–rGO (E_g 1.4 V) and then moves to the VB of In$_2$S$_3$ (1.54 V) and finally recombines with the holes of In$_2$S$_3$ as shown in Scheme 1. Thus, VB holes of In$_2$S$_3$ and CB electrons of BiOBr were annihilated efficiently preventing the photoexcited charge

carrier's recombination and consequently improving interfacial charge transmission. Moreover, the S–rGO offers a larger surface as well as SP^2 hybridization and π–π conjugation, considerably enhancing the mobility of photoinduced charge carriers between BiOBr and In$_2$S$_3$. Finally, the electrons from the CB of In$_2$S$_3$ are used to reduce Cr(VI), as shown in Scheme 1. Furthermore, the E_{CB} of In$_2$S$_3$ (−0.81 eV)[13,94] is substantially more negative than the Cr(VI) reduction potential (1.33 eV versus NHE[18]), thus, the photoinduced electrons at the CB of In$_2$S$_3$ can efficiently reduce Cr(VI) ions to Cr(III) ion. Similarly, the E_{VB} of BiOBr (2.65 eV)[59] is more positive than the reduction potential of O$_2$/H$_2$O (1.23 eV against NHE),[84] thus, the photoinduced holes at the VB of BiOBr can effectively oxidize 2H$_2$O to O$_2$ and 2H$^+$ simultaneously. The steps of the chemical reaction are presented as follows.

$$In_2S_3/BiOBr + hv \text{ (visible)} \rightarrow In_2S_3 \text{ } (e_{CB}^-) + BiOBr \text{ } (h_{VB}^+) \tag{10}$$

$$2H_2O + BiOBr \text{ } (4h_{VB}^+) \rightarrow O_2 + 4H^+ \tag{11}$$

$$Cr_2O_7^{2-} + 14H^+ + In_2S_3 \text{ } (6e_{CB}^-) \rightarrow 2Cr(III) + 7H_2O \tag{12}$$
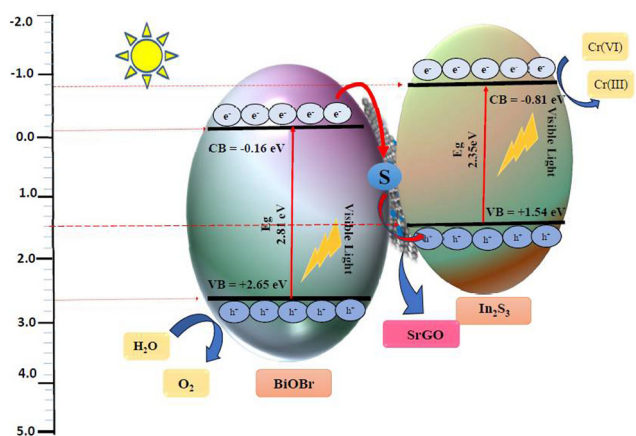
4. Conclusion

A novel BiOBr–In$_2$S$_3$–SrGO Z-scheme photocatalyst was prepared by a facile hydrothermal method. The XRD, FTIR, Raman, UV-Vis DRS, FE-SEM, HRTEM, EDAX, XPS and PL analysis verified that the nanocomposite was well prepared. The results reveal that at an initial 100 mg L^{-1} Cr(VI), almost 96.6% removal was achieved by the nanocomposite within 2 h under the illumination of solar light. Furthermore, the estimated apparent rate constant (K_{app}) of the nanocomposite for Cr(VI) reduction was found to be 3 times more than the individual NMs. This might be due to the efficient inhibition of electron–hole pair recombination, superior charge transfer by formation of a z scheme heterojunction, and application of S-doped rGO. FE-SEM of the nanocomposite proves the uniform distribution of rectangular 3D nanoplatelets of BiOBr and dense nanospheres of In$_2$S$_3$ anchored on the interconnected 3D porous S–rGO. The 3D nanoplatelet structure offers a greater surface area, while the exfoliated and corrugated S–rGO structure facilitates charge transfer and thus enhances photocatalytic activity. Furthermore, the BiOBr–In$_2$S$_3$–SrGO reveals outstanding stability and can be reused for several consecutive cycles. Therefore, this work offers a novel method for creating an effective Z-scheme photocatalyst system for treating Cr(VI)-contaminated wastewater and provides an excellent prospect for application in environmental and aquatic ecosystems.

Scheme 1 Mechanism of Cr(VI) reduction using the BiOBr–In$_2$S$_3$–SrGO nanocomposite.

Author contributions

Satyanjib Sahoo: methodology, conduct experiments and investigation, analysed sample data curation, writing – original draft, writing – review & editing, formal analysis. Naresh Kumar

Sahoo: conceptualization, methodology, investigation, visualization, writing – original draft, supervision, review & editing, resources, formal analysis, funding acquisition. Prasanta Kumar Sahoo: conceptualization, data curation, writing – original draft, formal analysis review & editing. Soumya Mishra: methodology, conduct experiments and investigation, analyzed sample, writing – review & editing. Arun Kumar: conduct experiments and investigation, analyzed sample, writing – review & editing. Rundaban Naik: investigation, conceptualization, data curation, writing – original draft, formal analysis review & editing. Prangyan Ranjan Rout: conceptualization, data curation, writing – original draft, formal analysis review & editing.

Data availability

Data will be made available on request.

Conflicts of interest

There are no conflicts to declare.

Acknowledgements

References

1 Y.-U. Shin, W. Pan, S. K. Patel, J. Lim, L. R. Winter, W. Ma, S. Hong and M. Elimelech, *Chem. Eng. J.*, 2023, **474**, 145756.

2 S. Singh, A. G. Anil, S. Khasnabis, V. Kumar, B. Nath, V. Adiga, T. S. S. Kumar Naik, S. Subramanian, V. Kumar, J. Singh and P. C. Ramamurthy, *Environ. Res.*, 2022, **203**, 111891.

3 M. Abinaya, K. Govindan, M. Kalpana, K. Saravanakumar, S. L. Prabavathi, V. Muthuraj and A. Jang, *J. Hazard. Mater.*, 2020, **397**, 122885.

4 G. Yuan, F. Li, K. Li, J. Liu, J. Li, S. Zhang, Q. Jia and H. Zhang, *Bull. Chem. Soc. Jpn.*, 2021, **94**, 1142–1155.

5 E. T. Anthony and N. A. Oladoja, *Environ. Sci. Pollut. Res.*, 2022, **29**, 8026–8053.

6 S. Mitra, A. Sarkar and S. Sen, *Nanotechnol. Environ. Eng.*, 2017, **2**, 11.

7 N. Doufar, M. Benamira, H. Lahmar, M. Trari, I. Avramova and M. T. Caldes, *J. Photochem. Photobiol., A*, 2020, **386**, 112105.

8 C.-C. Wang, X.-D. Du, J. Li, X.-X. Guo, P. Wang and J. Zhang, *Appl. Catal., B*, 2016, **193**, 198–216.

9 J. Zeng and Y. Huang, *Int. J. Hydrogen Energy*, 2024, **51**, 423–432.

10 L. Meng, Y. Qu and L. Jing, *Chin. Chem. Lett.*, 2021, **32**, 3265–3276.

11 J. Sun, C. Jiang, Z. Wu, Y. Liu and S. Sun, *Chemosphere*, 2022, **308**, 136107.

12 X. Zhong, Y. Liu, S. Wang, Y. Zhu and B. Hu, *Sep. Purif. Technol.*, 2021, **279**, 119627.

13 Y. Hua, C. Hu, M. Arif, S. Chen, M. Zhang and X. Liu, *J. Alloys Compd.*, 2022, **908**, 164488.

14 J. Singh and R. K. Soni, *Sci. Rep.*, 2021, **11**, 15352.

15 S. Bhattacharya, A. A. Das, G. Chandra Dhal, P. K. Sahoo, A. Tripathi and N. K. Sahoo, *J. Environ. Manage.*, 2022, **302**, 114022.

16 J. Li, Z. Ding, J. Li, C. Wang, L. Pan and G. Wang, *J. Chem. Eng.*, 2021, **407**, 127199.

17 Z. Jiang, F. Yang, G. Yang, L. Kong, M. O. Jones, T. Xiao and P. P. Edwards, *J. Photochem. Photobiol., A*, 2010, **212**, 8–13.

18 J. Luo, X. Zhou, X. Ning, L. Zhan, L. Ma, X. Xu, Z. Huang and J. Liang, *New J. Chem.*, 2017, **41**, 845–856.

19 Z. Tian, J. Li, G. Zhu, J. Lu, Y. Wang, Z. Shi and C. Xu, *Phys. Chem. Chem. Phys.*, 2015, **18**, 1125–1130.

20 P. Makuła, M. Pacia and W. Macyk, *J. Phys. Chem. Lett.*, 2018, **9**, 6814–6817.

21 G. Venkatesan and T. Subramani, *Indian J. Mar. Sci.*, 2019, **48**, 528–534.

22 J. Chen, X. Xiao, Y. Wang, M. Lu and X. Zeng, *J. Alloys Compd.*, 2019, **800**, 88–98.

23 G. D. O. Lima, T. P. Araujo, J. R. D. O. Lima, G. M. P. Prazeres, C. W. A. Paschoal, E. Longo, A. A. Tanaka, A. P. MacIel, D. A. B. Barbosa and M. A. P. Almeida, *Bol. Soc. Esp. Ceram. Vidrio*, 2021, **60**, 2–12.

24 Y. Wang, L. Lin, F. Li, L. Chen, D. Chen, C. Yang and M. Huang, *Photochem. Photobiol. Sci.*, 2016, **15**, 666–672.

25 M. Kraini, F. W. Aldbea, N. Bouguila and C. Vázquez-Vázquez, *J. Appl. Sci.*, 2018, 17.

26 G. R. Gopinath, R. W. Miles and K. T. Ramakrishna Reddy, *Energy Procedia*, 2013, **34**, 399–406.

27 M. Brahmayya, S.-Y. Suen and S. A. Dai, *J. Taiwan Inst. Chem. Eng.*, 2018, **83**, 174–183.

28 P. Kumar Sahoo, B. Panigrahy and D. Bahadur, *RSC Adv.*, 2014, **4**(89), 48563–48571.

29 S. S. Imam, R. Adnan, N. H. Mohd Kaus and M. H. Hussin, *J. Mater. Sci.: Mater. Electron.*, 2019, **30**, 6263–6276.

30 A. Alsulamei and A. Timoumi, *Opt. Mater.: X*, 2022, **15**, 100176.

31 A. Timoumi, W. Zayoud, A. Sharma, M. Kraini, N. Bouguila, A. Hakamy, N. Revaprasadu and S. Alaya, *J. Mater. Sci.: Mater. Electron.*, 2020, **31**, 13636–13645.

32 M. Toumi, N. Bouguila, B. Tiss, C. Dias, R. C. Veloso, M. Kraini, J. Ventura and S. Alaya, *Solid State Sci.*, 2022, **133**, 107021.

33 S. Hassanpoor and E. Tamri, *J. Alloys Compd.*, 2023, **932**, 167711.

34 J. Wang, Y. Zhang, L. Tian, F. Liu and Q. Xia, *J. Nanopart. Res.*, 2014, **16**, 2691.

35 T. Sall, A. Nafidi, B. M. Soucase, M. Mollar, B. Hartitti and M. Fahoume, *J. Semicond.*, 2014, **35**, 063002.

36 O. Surucu, M. Isik, M. Terlemezoglu, N. M. Gasanly and M. Parlak, *J. Mater. Sci.: Mater. Electron.*, 2021, **32**, 15851–15856.

37 M. Chaudhary, V. Doiphode, P. Shinde, A. Punde, P. Vairale, Y. Hase, A. Waghmare, M. Prasad and S. Jadkar, *Mater. Today: Proc.*, 2019, **vol. 39**, 1889–1893.

38 A. C. Ferrari, J. C. Meyer, V. Scardaci, C. Casiraghi, M. Lazzeri, F. Mauri, S. Piscanec, D. Jiang, K. S. Novoselov, S. Roth and A. K. Geim, *Phys. Rev. Lett.*, 2006, **97**, 187401.

39 J. Ji, G. Zhang, H. Chen, S. Wang, G. Zhang, F. Zhang and X. Fan, *Chem. Sci.*, 2011, **2**, 484–487.

40 C. Wu, C. Zhou, Y. Chen, Z. Peng, J. Yang and Y. Zhang, *J. Nanomater.*, 2021, **2021**, 1–14.

41 M. Jiang, Y. Zhang, J. Chen, Q. Liang, S. Xu, C. Yao, M. Zhou and Z. Li, *Cellulose*, 2020, **27**, 8843–8858.

42 L. Wang, B. Zhao, C. Wang, M. Sun, Y. Yu and B. Zhang, *J. Mater. Chem. A*, 2020, **8**, 10175–10179.

43 D. A. Bala, H. Ali, D. Eli and T. Yunana, *FUDMA J. Sci.*, 2019, **3**, 226–231.

44 S. S. Imam, R. Adnan and N. H. Mohd Kaus, *Appl. Sci.*, 2019, **1**, 845.

45 S. K. Sahoo, A. A. Das, D. Deka, B. Naik and N. Kumar Sahoo, *J. Mol. Liq.*, 2021, **339**, 116721.

46 A. Han, J. Sun, G. K. Chuah and S. Jaenicke, *RSC Adv.*, 2017, **7**, 145–152.

47 Y. Li, H. Jiang, X. Wang, X. Hong and B. Liang, *RSC Adv.*, 2021, **11**, 26855–26875.

48 A. R. Warrier, J. Bingi and C. Vijayan, *Plasmonics*, 2016, **11**, 953–961.

49 F. Saadallah, N. Jebbari, N. Kammoun and N. Yacoubi, *Int. J. Photoenergy*, 2011, **2011**, 1–4.

50 B. D. Ossonon and D. Bélanger, *RSC Adv.*, 2017, **7**, 27224–27234.

51 S. Wu, Y. Xie, X. Zhang, Z. Huang, Y. Liu, M. Fang, X. Wu and X. Min, *J. Mater. Res.*, 2019, **34**, 3450–3461.

52 L. Wang and L. Zan, *J. Nanopart. Res.*, 2020, **22**, 325.

53 M. Kraini, N. Bouguila, A. Bettaibi, J. Koaib, C. Vázquez-Vázquez, K. Khirouni, M. A. López-Quintela and S. Alaya, *J. Mater. Sci.: Mater. Electron.*, 2016, **27**, 11556–11564.

54 X. Fu, J. Tao, Z. He, Y. Gao, Y. Xia and Z. Zhao, *J. Alloys Compd.*, 2023, **936**, 168202.

55 X. Tu, S. Qian, L. Chen and L. Qu, *J. Mater. Sci.*, 2015, **50**, 4312–4323.

56 J. Shang, Y. Gao, B. Zhao, S. Shen and X. Wang, *J. Mater. Sci.: Mater. Electron.*, 2020, **31**, 20858–20867.

57 W. Huang, X. Hua, Y. Zhao, K. Li, L. Tang, M. Zhou and Z. Cai, *J. Mater. Sci.: Mater. Electron.*, 2019, **30**, 14967–14976.

58 Y. Hua, C. Hu, M. Arif, S. Chen, M. Zhang and X. Liu, *J. Alloys Compd.*, 2022, **908**, 164488.

59 W. Yao, D. Li, S. Wei, X. Liu, X. Liu and W. Wang, *ACS Omega*, 2022, **7**, 36479–36488.

60 A. M. Sadanandan, M. Fawaz, N. P. Dharmarajan, M. Huš, G. Singh, C. Sathish, B. Likozar, Z. Li, A. M. Ruban, C.-H. Jeon, J.-H. Yang, P. Kumar and A. Vinu, *Appl. Catal., B*, 2024, 124701.

61 J. Xu, B. Luo, W. Gu, Y. Jian, F. Wu, Y. Tang and H. Shen, *New J. Chem.*, 2018, **42**, 5052–5058.

62 T. Jia, J. Wu, Y. Xiao, Q. Liu, Q. Wu, Y. Qi and X. Qi, *J. Colloid Interface Sci.*, 2021, **587**, 402–416.

63 S. Fu, H. Zhu, Q. Huang, X. Liu, X. Zhang and J. Zhou, *J. Alloys Compd.*, 2021, **878**, 160372.

64 H. Chai, L. Gao, P. Wang, F. Li, G. Hu and J. Jin, *Appl. Catal., B*, 2022, **305**, 121011.

65 X. Ren, Y. Sun, H. Xing, K. Wu, W. Wang, J. Yin, S. Yao, X. Zhao and H. Yang, *J. Nanopart. Res.*, 2019, **21**, 111.

66 J. Park, T. H. Lee, C. Kim, S. A. Lee, M.-J. Choi, H. Kim, J. W. Yang, J. Lim and H. W. Jang, *Appl. Catal., B*, 2021, **295**, 120276.

67 H. Y. Hafeez, J. Mohammed, C. E. Ndikilar, A. B. Suleiman, R. S. Sa'id and I. Muhammad, *Ceram. Int.*, 2023, **49**, 5269–5278.

68 S. Choudhury, S. Pattnayak, U. Sahoo, P. Aparajita and G. Hota, *Ind. Eng. Chem. Res.*, 2023, **62**, 8191–8209.

69 X.-L. Luo, S.-Y. Yang, Z.-L. Wang and Y.-H. Xu, *Sep. Purif. Technol.*, 2023, **318**, 123966.

70 S. Habi Ben Hariz, H. Lahmar, G. Rekhila, A. Bouhala, M. Trari and M. Benamira, *J. Photochem. Photobiol., A*, 2022, **430**, 113986.

71 B. Dai, Y. Li, J. Xu, C. Sun, S. Li and W. Zhao, *Appl. Surf. Sci.*, 2022, **592**, 153309.

72 N. Khosroshahi, M. Bakhtian and V. Safarifard, *J. Photochem. Photobiol., A*, 2022, **431**, 114033.

73 N. Khosroshahi, M. D. Goudarzi, M. E. Gilvan and V. Safarifard, *J. Mol. Struct.*, 2022, **1263**, 132994.

74 V. Balakumar, C. Chuaicham, K. Sasaki and K. Sekar, *Mater. Today: Proc.*, 2021, **vol. 50**, 400–405.

75 A. Chachvalvutikul, T. Luangwanta and S. Kaowphong, *J. Colloid Interface Sci.*, 2021, **603**, 738–757.

76 R. Yang, Z. Zhu, C. Hu, S. Zhong, L. Zhang, B. Liu and W. Wang, *J. Chem. Eng.*, 2020, **390**, 124522.

77 A. Raja, P. Rajasekaran, K. Selvakumar, M. Arivanandhan, S. Asath Bahadur and M. Swaminathan, *ACS Omega*, 2020, **5**, 6414–6422.

78 X. Yuan, X. Wu, Z. Feng, W. Jia, X. Zheng and C. Li, *Catalysts*, 2019, **9**, 624.

79 G. Wu, Q. Liu, J. Wang, S. Xia, X. Huang, J. Han and W. Xing, *Colloids Surf., A*, 2022, **653**, 130048.

80 L. Luo, S. Dong, H. Cui, L. Sun and T. Huang, *J. Colloid Interface Sci.*, 2022, **606**, 1299–1310.

81 M. Yu, J. Shang and Y. Kuang, *J. Mater. Sci. Technol.*, 2021, **91**, 17–27.

82 D. S. Pattanayak, J. Mishra, J. Nanda, P. K. Sahoo, R. Kumar and N. K. Sahoo, *J. Environ. Manage.*, 2021, **297**, 113312.

83 S. C. Xu, Y. X. Zhang, S. S. Pan, H. L. Ding and G. H. Li, *J. Hazard. Mater.*, 2011, **196**, 29–35.

84 Z. Li, B. Liu, X. Zhang, C. Zhang, Y. Bai, J. Liu, Y. Wang, S. Yang, R. Li and C. Fan, *Sustainable Energy Fuels*, 2024, **8**, 262–271.

85 F. Sun, H. Ghosh, J. Wang, Z. Tan and S. Sivoththaman, *IEEE Trans. Nanotechnol.*, 2022, **21**, 481–488.

86 J. Zhang, L. Ding, W. Sun, W. Bi, Z. Wu and F. Gao, *J. Alloys Compd.*, 2021, **889**, 161770.

87 X. Fu, L. Wang, Z. He, Y. Gao, Y. Xia, J. Tao and Z. Zhao, *J. Solid State Chem.*, 2023, **319**, 123794.

88 Y. Wang, L. Qiu, S. Bao, F. Tian, L. He, W. Yang, Y. Liu and Y. Yu, *J. Chem. Eng.*, 2023, **468**, 143768.

89 X. Fu, L. Wang, F. Gao, C. Zhu, J. Tao, Z. He, Y. Xia and Z. Zhang, *Fuel*, 2024, **368**, 131700.

90 H. Gong, C. Bao, X. Luo, Y. Yu and W. Yang, *Microchem. J.*, 2024, **198**, 110109.

91 Y. Wang, S. Bao, X. Liu, L. Qiu, J. Sheng, W. Yang and Y. Yu, *J. Chem. Eng.*, 2023, **477**, 147050.

92 X. Guo, L. Qiu, M. Li, F. Tian, X. Ren, S. Jie, S. Geng, G. Han, Y. Huang, Y. Song, W. Yang and Y. Yu, *J. Chem. Eng.*, 2024, **483**, 149264.

93 L. Li, F. Tian, L. Qiu, F. Wu, W. Yang and Y. Yu, *Catalysts*, 2023, **13**, 1497.

94 X. Fu, J. Tao, Z. He, Y. Gao, Y. Xia and Z. Zhao, *J. Alloys Compd.*, 2023, **936**, 168202.